Inorganic Chemistry

Article

pubs.acs.org/IC

Novel Tailormade $Bi_4MO_4(PO_4)_2$ Structural Type (M = Mg, Zn)

Diana Endara,[†] Marie Colmont,*[,†] Marielle Huvé,[†] Grégory Tricot,[†] Laurent Carpentier,[‡] and Olivier Mentré[†]

[†]Université Lille 1, Université Lille Nord France, ENSCL, CNRS, UCCS, UMR 8181, F-59652 Villeneuve d' Ascq, France

[‡]CNRS, Unite Mat & Transformat UMET, UMR 8207, F-59655 Villeneuve D'Ascq, France

Supporting Information

ABSTRACT: In the Bi_2O_3−MO−P_2O_5 ternary system, the commonly observed sizable 1D ribbon-like units have been extended to their 2D infinite end member, leading to the novel tailormade $Bi_4MO_4(PO_4)_2$ compounds. It contains planar $[Bi_2O_2]^{2+}$ derivatives, separated by two slabs of PO_4, which create channels hosting the M^{2+} cations (M = Mg, Zn). For both compounds, supercell orderings occur comparatively to the predicted ideal crystal structure ($V_{Mg} = 2V_{ideal}$ and $V_{Zn} = 8V_{ideal}$). In the Mg case a transition into the ideal lattice occurs above 450 °C. In spite of the conceptual assembly of 2D motifs, the final architecture is three-dimensional due to strong interbonds. Thus, our work gives new insights on the possibility for versatile organization of original secondary building units (SBUs) able to self-assemble into predicted structural edifices. Single-crystal and powder XRD versus temperature, high-temperature ^{31}P NMR, as well as transmission electron microscopy were used for structural characterization. Preliminary electric characterization is also reported.

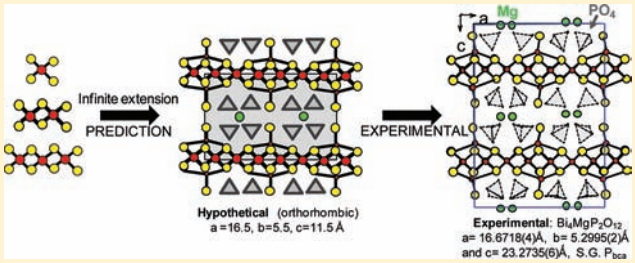

INTRODUCTION

Prediction of tailormade compounds is currently a major challenge in solid-state chemistry. On particular, self-assembly of SBUs proved its efficiency for elaboration of open-metal oxide frameworks (MOF).[1,2] Here, the organization between the inorganic units is mediated by organic ligands which link the inorganic units through flexible connections. However, the engineering of "pure" inorganic compounds remains a rare science and is generally restricted to the class of 2D layered compounds in which modular SBUs stack with respect to charge compensation and interfacial coherence.[3] For greater dimensionalities, an intuitive procedure consists of the a posteriori identification of phase homologies that leads to distinguishing common building units, to rationalize their connectivity, and to expansion of the system toward new members. A recent example of such megaseries, in which the structural and compositional principles are rationalized, is given by the 3D $A_m[M_{1+l}Se_{2+l}]_{2m}[M_{2l+n}Se_{2+3l+n}]$ and layered $(Sb_2Te_3)_m(Sb_2)_n$ compounds.[4,5]

In this context, we are interested in the organization of bismuth-based 1D sizable units into new XO_4-containing frameworks (X = P, As, V). Indeed, the Bi_2O_3−MO−P_2O_5 ternary system is known to be rich in terms of structural archetypes in competition. Structural filiations have been generalized with respect to pertinent SBUs and empirical structural rules.[6] The convenient description of the highlighted SBUs is based on the antistructure approach,[7−9] i.e., they are built on the association of $O(Bi,M)_4$ antitetrahedra sharing edges into 1D polycationic ribbons of variable size *n*, *n* being the number of tetrahedra along the finite ribbon dimension.[6] These SBUs are surrounded by PO_4 groups, while channels (hosting M^{2+} cations) can grow along the PO_4 walls. Strikingly, the structural prediction, formulation, and elaboration of novel archetypes have been successfully achieved for $n = 5$ and 11.[6] However, variously sized SBUs can also coexist in the materials, leading to the potentiality of numerous original members. Currently, the characterization of sizable SBUs from $n = 1$ to $n = 12$[6] suggests the possible stabilization of the infinite end members. It would correspond to 2D fluorine-$[Bi_2O_2]^{2+}$ derivatives arranged with PO_4 within two possible original crystal structures. In this paper, we predicted and elaborated one of those which corresponds to the formula $Bi_4MO_4(PO_4)_2$ (M = Mg, Zn). Complex superstructure, twinned phenomena, and phase transitions have been investigated by means of the combined use of X-ray diffraction (XRD) and transmission electron microscopy (TEM) and technically challenging in situ high-temperature ^{31}P NMR. Several bismuth oxide compounds show interesting dielectric properties and especially Aurivilius-phase materials. The interesting physical properties of such compounds (ferroelectric[10] state with high Curie temperature, piezoelectric properties,[11] etc.) make them intensively studied materials for electronic devices intended for operation under extreme conditions. In this context, preliminary electric characterization of the title compounds has been performed.

Received: July 26, 2011
Published: March 26, 2012

EXPERIMENTAL SECTION

Synthesis. Powder samples corresponding to compounds $Bi_4Zn_{(1-x)}Mg_xP_2O_{12}$ (x = 0−1) have been prepared by solid-state reaction between stoichiometric amounts of Bi_2O_3, MO (M = Zn and Mg), and $(NH_4)_2HPO_4$ at 850 °C for 96 h with several grinding steps. Colorless single crystals of $Bi_4ZnP_2O_{12}$ and $Bi_4MgP_2O_{12}$ were obtained by melting at 900 °C and subsequent slow cooling to room temperature (3 °C/h).

Powder XRD. Data were collected at room temperature using a D8 Advance Bruker AXS diffractometer and at high temperature (HTXRD) using a Bruker D8 diffractometer equipped with a high-temperature Anton Paar HTK 1200 N chamber and a one-dimensional X-ray detector (VANTEC-1), Cu Kα radiation. Data were collected from room temperature to 850 °C on heating and cooling.

Thermal Analysis. Thermogravimetric experiments have been carried out on a thermoanalyzer TGA 92 SETARAM under air with a heating rate of 5 °C·min^{-1} from room temperature to 1000 °C.

Single-Crystal X-ray Diffraction. Single-crystal X-ray diffraction data were collected using a Bruker X8 APPEX II diffractometer equipped with a fine-focus Mo target X-ray tube (λ = 0.71073 Å). Intensity data have been extracted from the collected frames using the program Saint Plus 6.02.[12] Lattice parameters were refined from the complete data set. Absorption corrections were performed for both compounds using SADABS.[12] Structure refinement has been performed with the JANA software.[13]

TEM. Electron diffraction patterns (EDP), images, and EDS results were obtained on a FEI Tecnai G220 transmission electron microscope equipped with a precession system and an EDS system. High-resolution images come from Geometrical Aberration Corrected-High ResolutionTransmission Electron Microscopy, FEI Titan. The material was crushed and dispersed on a holey carbon film deposited on a Cu grid.

Impedance Spectroscopy. Conductivity measurements were carried out on a broad frequency range (10^{-2}−10^6Hz) using the Novocontrol GMBH Alpha dielectric analyzer. Thermalization was performed in the 233−513 K temperature range every 20 K using a nitrogen-gas cryostat controlled by a Novocontrol Quatro cryosystem ensuring a temperature stability of better than 0.1 K. The sample (pellets, thickness ≈ 1 mm, density ≈ 80%) was placed between the two gold-plated electrodes of the BDS1308 liquid parallel plate cell (Θ = 20 mm).

^{31}P HT MAS NMR. ^{31}P in situ HT MAS NMR analyses were conducted from room temperature to 630 °C at 243 MHz on a 14.1 T Bruker spectrometer with a HT-MAS Bruker probehead equipped with a laser heating system and operating at a spinning frequency of 5 kHz. Experiments were recorded using a single-pulse acquisition scheme with a $\pi/2$ pulse length of 5.5 μs, 16 transients, and a rd of 20 s. The temperature inside the probehead was calibrated by following the temperature-dependent evolution of the ^{79}Br chemical shift on the KBr compound. All ^{31}P chemical shifts are given relative to 85% H_3PO_4 solution.

STRUCTURAL RULES AND PREDICTION OF NEW COMPOUNDS

State of the Art. In the concerned series of materials, the arrangement between polycationic ribbons (=SBUs) and PO_4 groups has been fully rationalized for cases dealing with intergrowths of one single nature of SBUs.[6] Systematic rules correlate the n size of SBUs and the full structural model, taking into account the cohesion between the ribbons and the PO_4 media, and allow a generic chemical formulation for real and hypothetical compounds. Three compounds with increasing n values (n = 2, 3, and 11) are shown in Figure 1 to appreciate the ribbons surrounded by PO_4. As previously evidenced, two cases have to be distinguished depending on the n size of the building ribbons.

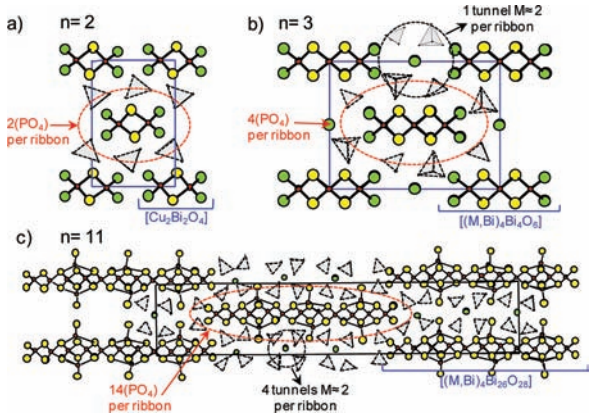

Figure 1. Structural rules and prediction of new compounds in the case of ribbons (a) n = 2, (b) n = 3, and (c) n > 3: n = 11. In each compound, the formulation of the ribbon and the corresponding number of surrounding phosphates and cations per tunnel are presented.

For n = 2 and 3,[14−21] the 1D polycations can be formulated $\{(M/Bi)_4Bi_{2n-2}O_{2n}\}^{x+}$ where M/Bi stands for the mixed edges of ribbons and Bi for their cores. In the plane perpendicular to the infinite axis of ribbons, we count $(2n - 2)$ PO_4 groups per ribbon. Cationic channels are created between phosphates for n = 3. It leads to the formulas $\{(M/Bi)^{edge}{}_4Bi^{core}{}_2O_4\}(PO_4)_2$ for n = 2 (Figure 1a for BiM_2PO_6) and $\{(M/Bi)^{edge}{}_4Bi^{core}{}_4O_6\}$-$(PO_4)_4M^{tunnel}{}_{\sim 2}$ for n = 3 (Figure 1b for $Bi_{\sim 1.2}M_{\sim 1.2}PO_{5.5}$).

For n > 3,[6,22] cohesion with the surrounding PO_4 groups is achieved by $(O-Bi)^+$ excrescences (= Ex) capping the ribbons every three $O(Bi/M)_4$ tetrahedra. The extra oxygen atoms are pentacoordinated (four Bi from the ribbons and one extra Bi). We recently established[6] the general formula of long-sized ribbons as $\{(M/Bi)^{Edge}{}_4Bi^{Core}{}_{2n-2}Bi^{Ex}{}_{2int[(n-1)/3]}O_{2n+2int[(n-1)/3]}\}^{x+}$ with $2((n - 1) - int[(n - 1)/3])$ PO_4 per ribbon. Here, int[x] denotes the integer part of x. For determination of the number of created tunnels, two cases should be distinguished depending on the existence or not of tunnels.

(i) $n \neq 3n'$: there are $int[(n + 1)/3] - 1$ tunnels per ribbon, which leads to the compounds formulated $\{ribbon\}_1$-$(PO_4)_{2((n-1)-int[(n-1)/3])}$ $M^{tunnel}{}_{\sim 2int[(n+1)/3]-1}$. This case is illustrated for n = 11 in Figure 1c.

(ii) $n = 3n'$: there are $n/3$ tunnels per ribbon, which leads to the compounds formulated $\{ribbon\}_1$-$(PO_4)_{2((n-1)-int[(n-1)/3])}$ $M^{tunnel}{}_{\sim 2n/3}$.

Toward the Infinite Term with Two Plausible Polymorphs. Starting from the crystal structure of the $Bi_{57.28}Zn_{7.976}Li_{8.208}(PO_4)_{28}O_{56}$[6] compound shown in Figure 1c (n = 11 term), one could easily extend the length of ribbons until infinite planes as schematized in Figure 2. To tackle this issue, SBUs deduced from observation of parent compounds were used. From the formulas developed for n > 3 (taking into account the regular alternation of $(O-Bi)^+$ and PO_4^{3-} groups), the infinite extension[23−26] leads to $\{Bi^{Core}{}_2Bi^{Ex}{}_{2n/3}O_{2n+2n/3}\}^{x+}(PO_4)_{4n/3}M_{\sim 2n/3}$ which is simplified to $\{Bi_4O_4\}M_{\sim 1}(PO_4)_2$. Mathematically, it is striking that for any n value ($n = 3n'$, case (i) above, or $n \neq 3n'$, case (ii) above) the infinite extension of n yields an identical amount of PO_4 groups and delimited tunnels. In the case of M^{2+} electroneutrality is reached for a stoichiometric amount of M^{2+} cations in the tunnels, which means that the tunnels would be supposedly totally filled (two M^{2+} in a tunnel period of ∼5.5 Å). In addition,

dx.doi.org/10.1021/ic201572y | Inorg. Chem. 2012, 51, 4438−4447

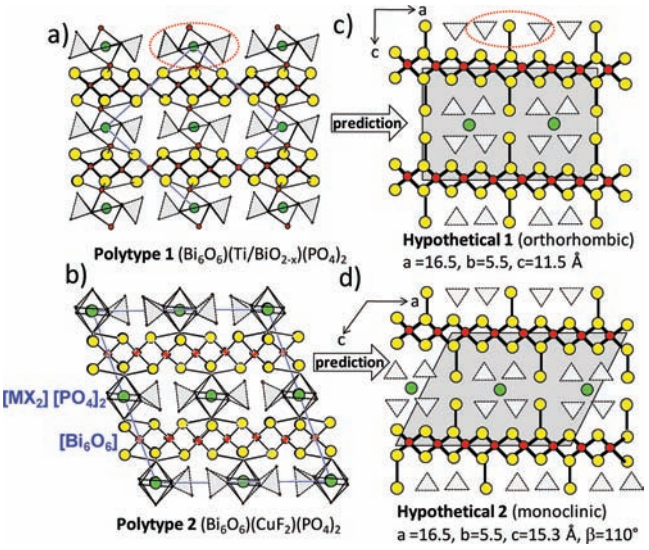

Figure 2. Infinite terms of $Bi_6O_6(Bi/MO_2)(PO_4)_2$ obtained as (a) polytype 1 and (b) polytype 2 in which infinite $[Bi_2O_2]^{2+}$ layers are surrounded by $[MO_2](PO_4)_2$ slabs and the predicted structure in which infinite $[Bi_2O_2]2+$ layers are surrounded by two rows of phosphate and cations: $(PO_4)_2MBi_2O_2]^{2-}$, (c) case of the zinc cations with two type of dimers in tunnels presented in the insert, and (d) Mg cations with one type on dimers in tunnels.

without counting the $(O-Bi)^+$ excrescences, the infinite ribbons would consist of the standard $[Bi_2O_2]^{2+}$ planes commonly found in Aurivilius compounds, sandwiched by perovskite slabs of various thickness.[25−27] In fact, examples of structures containing these $[Bi_2O_2]^{2+}$ planes separated by tetrahedral XO_4 groups have been already identified in the past for $Bi_6O_6(VO_2)(VO_4)_2$ (see Figure 2a, with TiO_2 and PO_4 replacing VO_2 and VO_4)) resulting from the reduction under flowing hydrogen of $Bi_4V_2O_{11}$[28,29] (at the head of the ionic-conducting BIMEVOX series). In the latter the reduced oxygen-deficient $[VO_{3.33}]^{2+}$ slabs consist of one VO_6 octahedron (O_h) and two VO_4 tetrahedra (T_d), see Figure 2a. Two variants of this crystal structure have been recently reported in the $Bi_2O_3-MO-P_2O_5$ system (M = Ti^{4+}, Fe^{3+}, Mn^{3+}, Ni^{2+}),[23,27] called polytypes 1 and 2 (Figure 2a and 2b). They differ from one another by the shifting between the $[2T_d-1O_h]$ layers at both sides of the central $[Bi_2O_2]^{2+}$ (see Figure 2a and 2b). In these compounds, a striking point concerns the possible partial substitution of the O_h site by Bi^{3+} as in $Bi_6O_6(Bi/TiO_{2-x})(PO_4)_2$, reminiscent of the $(O-Bi)^+$ excrescences. Then, the simple analogy between these two polytypes and the targeted compound would also drive to two possible polymorphs, taking into account the different shift of the $(O-Bi)^+$ excrescences and PO_4 around $[Bi_2O_2]^{2+}$ planes. The expected unit cell for the symmetry of the hypothetical model 1 (alignment of the $(O-Bi)^+$) should be orthorhombic with theoretical parameters around a_1 = 16.5 Å, b_1= 5.5 Å, and c_1 = 11.5 Å from our previous investigations of several related compounds, Figure 2c. In the case of misaligned $(O-Bi)^+$ excrescences (hypothetical model 2), the symmetry would be lowered to monoclinic with ideal lattice constants a_2 = 16.5 Å, b_2 = 5.5 Å, c_2 = 15.3 Å, and β_2 = 110°; see Figure 2d.

The syntheses of the expected $\{Bi_4O_4\}M_1(PO_4)_2$ compositions have been tested for M = Cd, Zn, Mg, and Cu, but only Zn and Mg yield the expected compounds as verified by the crystal structure refinement detailed below.

RESULTS AND DISCUSSION

Single crystals have been obtained from melting and slow cooling of polycrystalline samples with the nominal composition $Bi_4MO_4(PO_4)_2$ (M = Zn and Mg). The crystallographic data are as follows.

$Bi_4MgO_4(PO_4)_2$: a = 16.6718(4) Å, b = 5.2995(2) Å, and c = 23.2735(6) Å, space group *Pbca*, R_1 = 0.0319, and wR_2= 0.0299 corresponds to a supercell of the model 1 with parameters a_1, b_1, $2c_1$.

$Bi_4ZnP_2O_{12}$: a = 33.5044(3) Å, b = 10.8211(9) Å, c = 27.6486(2) Å, and β = 121.892(4)°, space group $C2/c$, R_1 = 0.0438, wR_2 = 0.0442. In addition to the monoclinic symmetry assorted with this compound, it is characterized by the doubling of two lattice parameters ($a_{Zn} \approx 2a_{Mg}$, $b_{Zn} \approx 2b_{Mg}$, which corresponds to 8 $V_{model\ 1}$), which prefigures complex superstructure phenomena. The lattice constants and space groups have been verified by electron diffraction for the corresponding powders after reconstitution of the reciprocal space for the two compounds. According to the method of Morniroli et al.[30] the partial extinction symbols were deduced from comparison of the shift and difference of periodicity between the zero- and the first-order Laue Zone and are compatible with the space group deduced from XRD (Figure 3). For the monoclinic cell (M = Zn), a shift and a

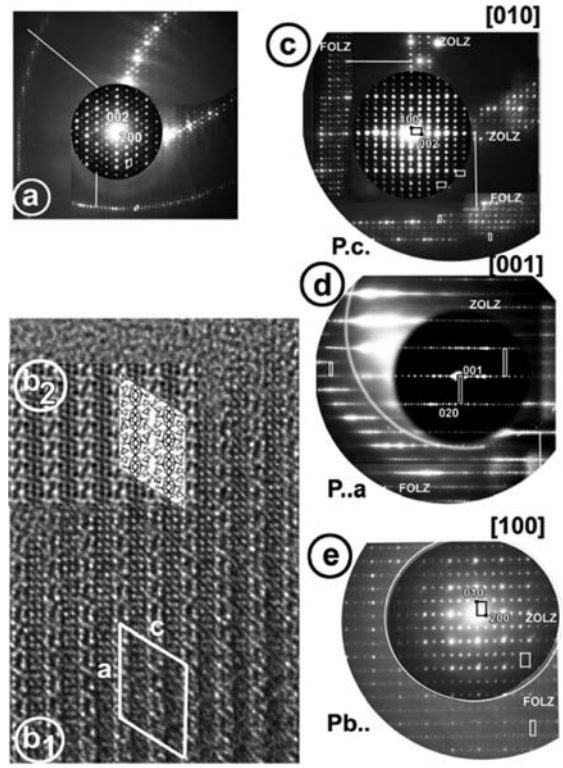

Figure 3. (a and b) $Bi_4ZnO_4(PO_4)_2$ sample: (a) [010] zone axis pattern, a shift and a difference of periodicity leads to a C1c1 extinction symbol, (b_1) corresponding HR image and (b_2) simulated image for a thickness of 21.6 Å and a defocus of −100 Å. (c, d, and e) $Bi_4MgP_2O_{12}$ sample [010], [001], and [100] zone axis patterns. Comparison of the shifts and difference of periodicity between reflections in the ZOLZ and FOLZ leads to the *Pbca* extinction symbol.

difference of periodicity along a on the [010] zone axis pattern (ZAP) leads to a C1c1 partial extinction symbol (Figure 3.a).

dx.doi.org/10.1021/ic201572y | *Inorg. Chem.* 2012, 51, 4438−4447

The corresponding high-resolution image shows a regular stacking sequence and a good correlation between calculated/observed images and the structural model described below (Figure 3b). For the orthorhombic cell (M = Mg), no shift but a difference of periodicity along *a*, *b*, *c* is observed on the basic [010], [001], [100] ZAP, leading to a *Pbca* partial extinction symbol (Figure 3c–e).

Pertinent data of the XRD data collection and structural refinement are summarized in Table 1. The heavy atoms were located using the Patterson approach, while the remaining atoms were deduced from difference Fourier maps.

Table 1. Crystal Data, Measurement, and Structure Refinement Parameters for $Bi_4ZnO_4(PO_4)_2$ and $Bi_4MgO_4(PO_4)_2$

	Crystal Data	
compound	$Bi_4ZnO_4(PO_4)_2$	$Bi_4MgO_4(PO_4)_2$
cryst symmetry	monoclinic	orthorhombic
space group	*C*2/*c* (no. 15)	*Pbca* (no. 61)
unit cell	*a* = 33.5044(3) Å	*a* = 16.6718(4) Å
	b = 10.8211(9) Å	*b* = 5.2995(2) Å
	c = 27.6486(2) Å	*c* = 23.2735(6) Å
	β = 121.892(4)°	
volume (Å^3)	8510.9(8)	2056.265
Z	32	8
M_w, calcd density (g/cm^3)	1155.2, 7.2103	1140.1, 7.905
F(000)	15 609	3758
	Data Collection	
equipment	Bruker X8	Bruker X8
tadiation Mo K*α* (Å)	0.71073	0.71073
scan mode	*ω*/*φ* scan	*ω*/*φ* scan
recorded angular range *θ* (deg)	1.43/36.28	1.75/32.86
recording reciprocal space	−55 ≤ h ≤55	−25 ≤ *h* ≤25
	−18 ≤ *k* ≤ 18	−8 ≤ *k* ≤ 6
	−46 ≤ *l* ≤ 46	−35 ≤ *l* ≤ 35
no. of measd reflns	338 026	32 350
no. of independent reflns	20 533	3819
no. of independent reflns [$I > 3\sigma(I)$]	14 481	2540
μ (cm^{-1}) (*λ* = Mo K*α*)	68.531	68.638
abs corr	empirical (Sadabs)	empirical (Sadabs)
transmission T_{min}/T_{max}	0.38	0.43
R merging factor (%)	8.65	8.38
	Refinement Parameters	
software, refinement type	Jana2000, L.S. on F	Jana2000 L.S. on F
no. of refined params	432	98
R_1 (F) all, $[I > 3\sigma(I)] = \sum\|\|F_o\| - \|F_c\|\|/\sum\|F_o\|$ (%)	0.0700/0.0438	0.0579/0.0319
wR_2 (F^2) all, $[I > 3\sigma(I)] = [\sum w(F_o^2 - F_o^2)^2/\sum w(F_o^2)]^{1/2}$ (%)	0.0681/0.0442	0.0338/0.0299
goodness of fit	1.35	1.18
weight	unit	unit
isotropic secondary extinction	304(5) × 10^{-5}	310(11)× 10^{-5}
max/min Δ*ρ*, e/Å^3	10.73/−5.37	3.8/−2.76

Crystal Structure Refinements. Two particular features are highlighted during the refinement process, compared to most of the "disordered" compounds previously isolated in similar chemical systems. First, PO_4 are fully ordered, while generally strong residual densities persist even after introduction of several O_4 shells around P atoms in related compounds (see, for instance, ref 27). Also, the M cations are ordered inside the 1D channels. It yields the $Bi_4MP_2O_{12}$ formula (M = Mg, Zn). EDS analysis performed on 20 crystals leads to average compositions of $Bi_4Mg_{0.7}P_{1.9}$ and $Bi_4Zn_{0.8}P_{1.8}$, which is in accordance with the structural formula. For both compounds, the pertinent distances at room temperature are given in the Tables 2 and 3. The refined atomic positions and isotropic and anisotropic displacement parameters are given in the Supporting Information. We note a significant residual electron density peak (∼10 e/Å^3) close to a Bi position in the Zn compound. This behavior is rather commonly observed around heavy atoms and could picture the presence of defects or imperfect absorption corrections. Several twin laws have been introduced but did not recover this effect. The representation of the two crystal structures is shown in Figure 4. It is based on $[Bi_2O_2]^{2+}$ planes sandwiched between $[(PO_4)_2MBi_2O_2]^{2-}$ double slabs. As stated for the *n* = 11 term,[4] a complex set of interaction between Bi^{3+} cations and lone pairs is expected to stabilize the interleave space.

For M = Mg, the main framework is isomorphous with expected hypothetical model 1. Only one independent Mg atom is located in the tunnels, surrounded by two independent PO_4 groups. Here the Mg^{2+} cations are arranged in zigzag chains growing along the *b* axis (Figure 4b). Their coordination is octahedral with Mg–O distances between 2.03 and 2.19 Å.

For M = Zn, despite the misleading analogy of lattice parameters with predicted model 2, the crystal structure also corresponds to model 1, somewhat distorted as detailed below. The doubling of the *b* axis is due to the existence of four independent Zn atoms ordered in each tunnel. Two kinds of Zn_2 dimers appear (Figure 4a): (i) the first one consists of $Zn1Zn2O_7$ tetrahedral pairs sharing a corner (dZn1–Zn2 = 3.45(1)Å, 1.88 Å < Zn–O < 2.01 Å); (ii) the second one consists of $Zn3Zn4O_9$ pairs in which the triangular-bipyramidal $Zn3O_5$ share one corner with the square-pyramidal $Zn4O_5$ (dZn3–Zn4 = 3.39(2)Å, 1.91 Å < Zn–O < 2.75 Å). The main difference between the occupancy of the tunnels in the two phases results from the ability of Zn to adopt both IV and V coordination, contrary to the magnesium compound that prefers the VI configuration. This observation is in opposition to what has been previously observed in $BiMg_2PO_6$[14] and $BiZn_2PO_6$[18] in which Mg and Zn both adopt pentacoordination (V). The doubling of the *a* axis compared to the predicted ideal case is explained by a slightly different rotation of one-half of the PO_4 groups against the other half.

It is striking that in both compounds the unit cell contains two $[Bi_2O_2]^{2+}$ layers related by symmetry operations and at the origin of the *a*-axis doubling. Another important point deals with the position of Bi atoms. In fact, in the Mg compound, two opposite interstitial O–Bi excrescences atoms are well aligned perpendicularly to the $[Bi_2O_2]^{2+}$, whereas in the case of Zn compounds, slight misalignment accompanies the symmetry loss from orthorhombic to monoclinic. However, apart from these slight differences both compounds show similarity with predicted model 1 rather than polytype 2 in terms of the alignment of their O–Bi excrescences.

Zn/Mg Miscibility. Synthesis of compounds of the solid solution $Bi_4Zn_{1-x}Mg_xP_2O_{12}$ (*x* = 0, 0.25, 0.5, 0.75, and 1) has been attempted, and the corresponding XRD show two defined domains. The first one (*x* = 0–0.25) corresponds to the Zn type. The second one (*x* = 0.5–1) yields the Mg type. The

dx.doi.org/10.1021/ic201572y | Inorg. Chem. 2012, 51, 4438–4447

Table 2. Selected Bond Distances (Angstroms) for $Bi_4ZnO_4(PO_4)_2$

atom 1	atom 2	distance (Å)	atom 1	atom 2	distance (Å)	atom 1	atom 2	distance (Å)	atom 1	atom 2	distance (Å)
P−O distances											
P1	O34	1.513 (8)	P2	O45	1.51 (2)	P3	O26	1.510 (4)	P4	O42	1.50 (2)
	O41	1.525 (3)		O37	1.526 (7)		O21	1.524 (6)		O44	1.512 (3)
	O40	1.544 (7)		O46	1.54 (2)		O25	1.529 (8)		O39	1.54 (2)
	O38	1.57 (2)		O30	1.577 (3)		O23	1.561 (6)		O24	1.570 (4)
P5	O47	1.51 (2)	P6	O49	1.500 (7)	P7	O48	1.514 (6)	P8	O33	1.505 (2)
	O50	1.522 (7)		O32	1.527 (6)		O43	1.529 (7)		O22	1.525 (6)
	O18	1.522 (7)		O28	1.530 (6)		O36	1.535 (9)		O27	1.526 (7)
	O35	1.54 (2)		O19	1.554 (7)		O29	1.562 (6)		O31	1.544 (7)
Zn−O distances											
Zn1	O44	1.897 (6)	Zn2	O48	1.920 (3)	Zn3	O28	1.910 (8)	Zn4	O49	1.89 (2)
	O34	1.91 (2)		O40	1.94 (2)		O35	1.920 (3)		O24	1.969 (3)
	O21	1.910 (1)		O30	1.984 (3)		O23	2.011 (5)		O30	2.028 (4)
	O27	2.018 (4)		O27	1.996 (5)		O29	2.017 (5)		O35	2.060 (9)
	O22	2.976 (9)					O48	2.735 (6)		O50	2.23 (2)
O−Bi distances							O21	2.925 (4)		O46	2.985 (8)
O1	Bi8(*2)	2.217 (8)	O2	Bi3(*2)	2.289 (8)	O11	Bi4	2.173 (5)	O12	Bi13(exc)	2.065 (3)
	Bi14(*2)	2.388 (8)		Bi1(*2)	2.366 (8)		Bi2	2.223 (5)		Bi16	2.272 (1)
O3	Bi8(*2)	2.235 (1)	O4	Bi3(*2)	2.198 (8)		Bi9	2.252 (1)		Bi1	2.465 (6)
	Bi1(*2)	2.405 (1)		Bi14(*2)	2.447 (8)		Bi15	2.67 (1)		Bi2	3.369 (3)
O5	Bi14	2.216 (1)	O6	Bi2	2.27 (1)					Bi15	3.378 (1)
	Bi10	2.276 (1)		Bi7	2.281 (4)	O13	Bi11(exc)	2.069 (3)	O14	Bi7	2.22 (1)
	Bi3	2.276 (5)		Bi12	2.298 (1)		Bi4	2.321 (1)		Bi16	2.228 (1)
	Bi16	2.492 (4)		Bi9	2.411 (4)		Bi9	2.464 (7)		Bi2	2.267 (4)
O7	Bi8	2.201 (4)	O8	Bi12	2.276 (1)		Bi8	3.474 (3)		Bi4	2.621 (4)
	Bi14	2.219 (1)		Bi7	2.279 (1)		Bi10	3.258 (1)			
	Bi15	2.222 (4)		Bi2	2.294 (1)	O15	Bi1	2.204 (1)	O16	Bi12	2.215 (5)
	Bi10	2.60 (1)		Bi9	2.404 (5)		Bi4	2.208 (1)		Bi7	2.222 (1)
O9	Bi15	2.212 (1)	O10	Bi16	2.182 (3)		Bi8	2.306 (4)		Bi10	2.246 (5)
	Bi9	2.224 (1)		Bi3	2.209 (3)		Bi15	2.674 (4)		Bi16	2.649 (1)
	Bi12	2.319 (5)		Bi1	2.223 (1)	O17	Bi5(exc)	2.052 (4)	O20	Bi6(exc)	2.024 (2)
	Bi10	2.568 (5)		Bi4	2.738 (1)		Bi10	3.525 (1)		Bi3	3.199 (6)
	Bi15	2.272 (1)		Bi10	2.193 (2)		Bi12	3.62 (1)		Bi16	3.642 (1)
	Bi14	2.365 (6)		Bi7	2.754 (9)						

Table 3. Selected Bond Distances (Angstroms) for α-$Bi_4MgO_4(PO_4)_2$

atom 1	atom 2	distance (Å)	atom 1	atom 2	distance (Å)
P−O distances					
P1	O11	1.526 (6)	P2	O12	1.531 (6)
	O7	1.543 (6)		O9	1.534 (6)
	O10	1.512 (6)		O5	1.555 (7)
	O6	1.561 (6)		O8	1.522 (6)
Mg−O distances					
Mg1	O8	2.035 (7)	Mg1	O10	2.086 (7)
	O8	2.053 (6)		O5	2.134 (6)
	O10	2.045 (6)		O6	2.193 (6)
O−Bi distances					
O1	Bi3	2.155 (7)	O2	Bi2	2.180(7)
	Bi2	2.217 (7)		Bi3	2.290 (7)
	Bi1	2.287 (7)		Bi1	2.322 (7)
	Bi3	2.593 (7)		Bi3	2.424 (7)
O3	Bi1	2.212 (7)	O4	Bi4 (exc)	2.039 (7)
	Bi1	2.321 (7)		Bi3	2.334 (8)
	Bi2	2.354 (7)		Bi2	2.635 (8)
	Bi2	2.363 (7)		Bi3	3.302 (8)
				Bi1	3.265 (8)

refined lattice parameters and parent-structural type are listed in the Supporting Information. The refined lattice parameters gradually decrease on increasing x, in agreement with the smaller ionic radii of Mg^{2+}. Due to the rare disposition of M in the tunnels, $Bi_4M_{1-x}Cu_xP_2O_{12}$ (M = Mg and Zn) compounds were prepared but did not lead to single-phase materials. At least in our synthesis conditions it seems that incorporation of Cu^{2+} is difficult probably due to strong constraints necessary to create square planar coordination from the PO_4 tunnel walls.

Analysis of Defects by TEM. Images of the Mg polycrystalline sample show a regular stacking periodicity in extended domains. In the Zn sample, the [010] ZAP of some crystals exhibits a splitting of the spots (Figure 5a) with increasing separation at higher diffraction angles, which suggests the occurrence of pseudomerihedral twins. The corresponding image reveals two domains bended by about 10°. In fact, the minor domain corresponds to a stripe of thickness ∼10 nm, Figure 5b. Analysis of the antiphase boundary passes through the use of the pseudo-orthorhombic cell defined for model 1 (Figure 2c, shown in red in Figure 5b). The twin operation corresponds to the pseudo-mirror perpendicular to the a axis applied to the monoclinic domains (Figure 5c). At the twin boundary, the juxtaposition of two mirror-related domains leads to slight deviation of the ribbon-propagation axis within a coherent interface, Figure 5d. It highlights the versatile adaptability of the 2D framework and great probability for various twins and intergrowths. However,

dx.doi.org/10.1021/ic201572y | Inorg. Chem. 2012, 51, 4438−4447

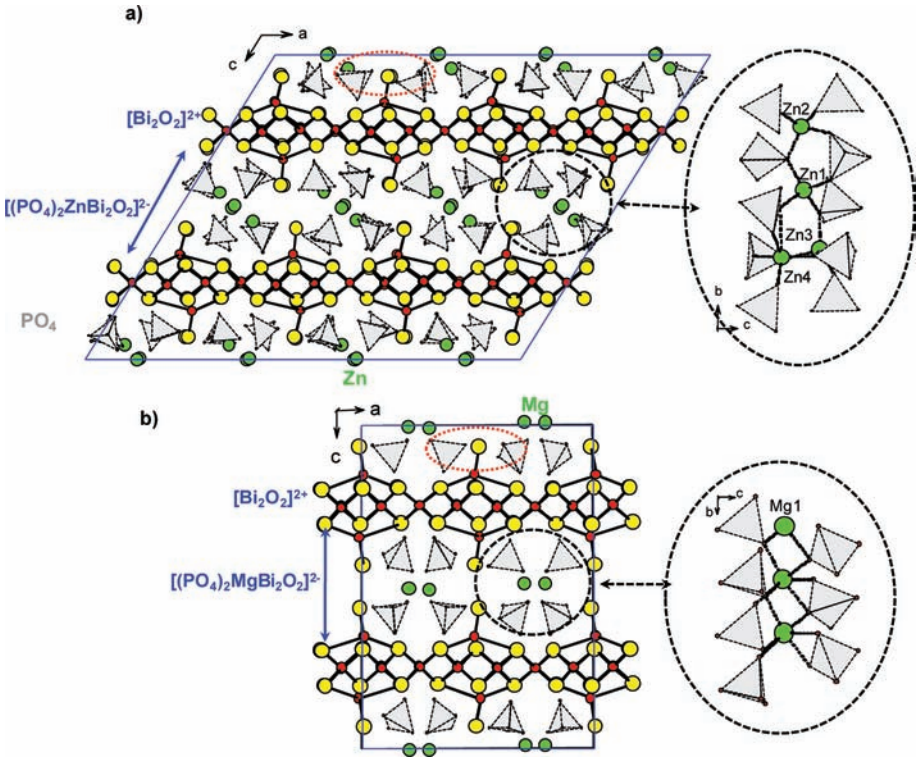

Figure 4. Crystal structure of $Bi_4MO_4(PO_4)_2$ with (a) M = Zn and (b) M = Mg. Arrangement of atoms in tunnels is presented in insert in both cases.

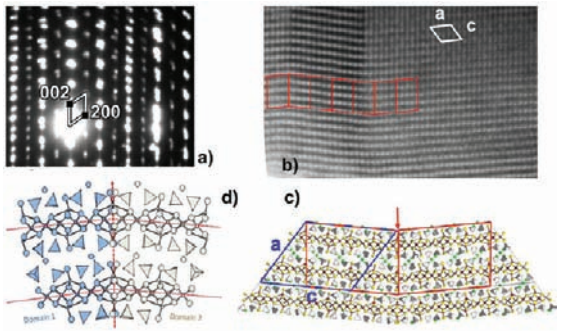

Figure 5. (a) [010] ZAP of $Bi_4ZnO_4(PO_4)_2$ sample showing a splitting of spots, (b) corresponding image shows domains bended by 10° due to the (c) result of twinning. (d) Paste of the two-domain leads at the level of the boundary to a perfect structural coherence except at the level of the excrescence which are slightly flipped.

on the single crystal used for the $Bi_4ZnP_2O_{12}$ crystal structure determination, no significant twinned domains were evidenced..

High-Temperature Structural Transitions. XRD study versus temperature was performed until 850 °C in order to check the stability of both Zn and Mg phases and the possible transition to higher symmetries. Results are gathered in Figure 6.

Zn Compound. The obtained XRD diagrams show no phase decomposition until 850 °C. The evolution of the unit cell parameters indicates a progressive lattice dilatation upon heating. However, an anomaly is observed around 270 °C that corresponds to an exothermic peak detected on DTA (Figure 6c). The supercell peaks distinguishable on XRD patterns ($2a_{ideal}$, $2c_{ideal}$ adapted to the monoclinic cell) persist across the transition which indicates that this rearrangement is of minor

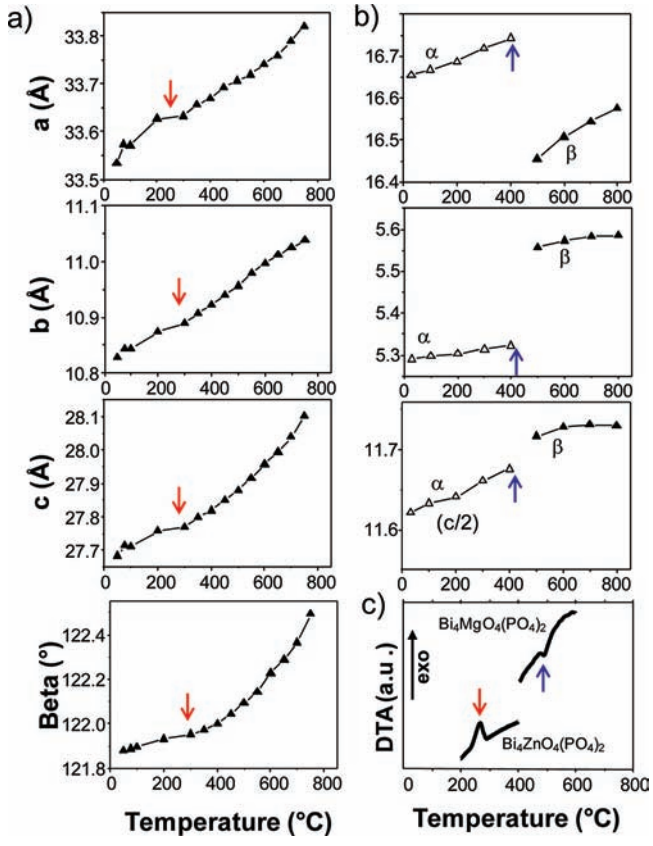

Figure 6. Evolution of lattice parameters versus temperature and visualization of the phase transition for (a) $Bi_4ZnO_4(PO_4)_2$ and (b) $Bi_4MgO_4(PO_4)_2$, and (c) DTA plot for the two compounds.

dx.doi.org/10.1021/ic201572y | Inorg. Chem. 2012, 51, 4438–4447

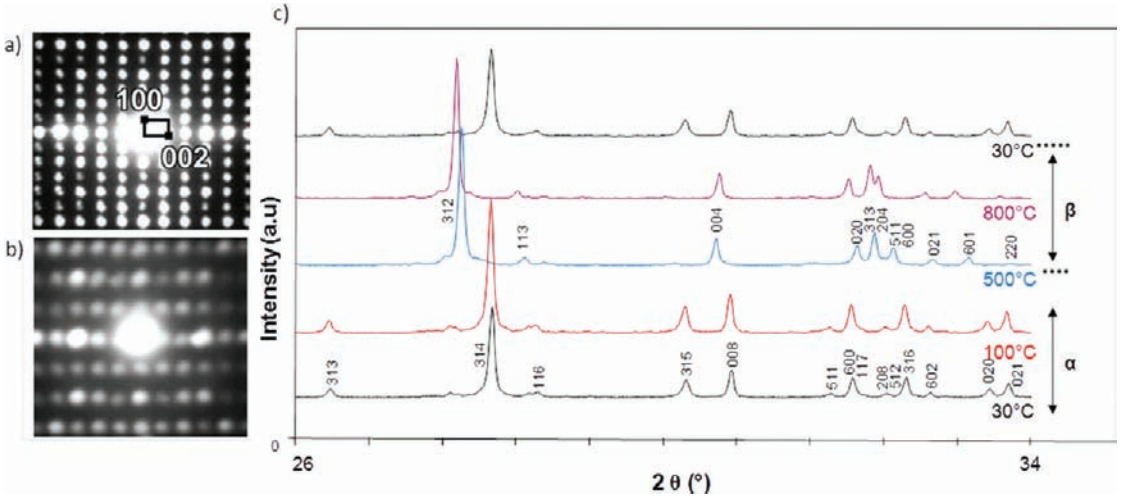

Figure 7. $Bi_4MgO_4(PO_4)_2$: [010] ZAP at (a) room temperature and (b) 500 °C, and (c) XRD patterns taken at various temperatures. $\alpha \rightarrow \beta$ transition observed at 500 °C is evidenced on ED t the extinction of odd h spots along (100).

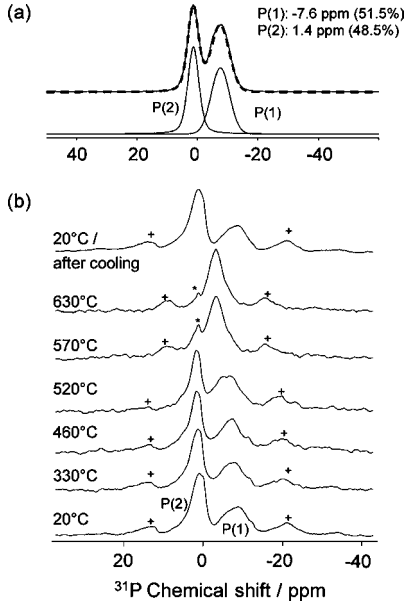

Figure 8. (a) ^{31}P MAS NMR analyses performed at 9.4 T accompanied with the simulation obtained with a two-site system (dashed line) and NMR parameters deduced from the simulation. (b) ^{31}P in situ HT MAS NMR analyses performed at 14.1 T between 20 and 630 °C. Spinning sidebands and impurity are denoted with + and *, respectively.

amplitude. The diffraction lines corresponding to the $2b_{ideal}$ ordering are too weak to be distinguished on powder XRD patterns such that one could not conclude about this particular direction. Due to the presence of a number of weak supercell satellites at both sides of the transition the high-temperature structure of $Bi_4ZnP_2O_{12}$ was not investigated. The thermal dependence of the lattice constants are shown in Figure 6a and leads to the mean thermal expansion coefficients $(1/L_0(\Delta L/\Delta T))$ along the three crystallographic dimensions: α_a = 12.10^{-6}, α_b = 27.10^{-6}, α_c = 21.10^{-6} (K^{-1}). Note that α_b appears exaggerated, which corresponds to the tunnel-growth axis. It prefigures a slight distortion of the Zn coordination by reorganization of the tunnel walls (rotation of the phosphate).

Table 4. Selected Bond Distances (Ansgtroms) for β-$Bi_4MgO_4(PO_4)_2$

atom 1	atom 2	distance (Å)	atom 1	atom 2	distance (Å)
P−O distances			Mg−O distances		
P1	Op3	1.549 (2)	Mg	Op1(*2)	1.934 (2)
	Op1	1.550 (1)		Op1(*2)	2.056 (2)
	Op4	1.552 (1)		Op2(*2)	2.373 (1)
	Op2	1.549 (2)			
O−Bi distances					
O1	Bi1(*2)	2.213 (1)	O2	Bi2 (exc)	2.259 (2)
	Bi1(*2)	2.469 (2)		Bi3	2.692 (4)
				Bi1(*2)	2.877 (2)
O3	Bi1	1.910 (2)			
	Bi3	2.521 (1)			
	Bi3	2.597 (2)			
	Bi1	2.469 (2)			

β Form of the Mg Phase. On the other hand, the HT-XRD patterns of $Bi_4MgP_2O_{12}$ show a brutal endothermic transition between 450 and 500 °C from the room-temperature α phase to the high-temperature β phase (Figure 6b and 6c). It is accompanied by the reversible vanishing of the supercell lines ($2a_{ideal}$,b,c). Additionaly, the ED of the [010] ZAP heated at about 500 °C confirms the disappearance of the $h0l$, $h = 2n + 1$ spots into the ideal predicted orthorhombic unit cell $a \approx 16$ Å, $b \approx 5$ Å, $c \approx 11$ Å, Figure 7a and 7b.

The $\alpha \rightarrow \beta$ transition passes through a brutal rearrangement of the phosphate groups in order to adopt the fundamental subcell. At room temperature, the ^{31}P MAS NMR spectrum (Figure 8a) shows the presence of two distinct phosphorus sites (centered at 1.3 and −7.6 ppm) in similar proportions, in good agreement with the crystallographic data. The high-field signal (at −7.6 ppm) exhibits a larger broadness compared to the other site (7.1 against 4.4 ppm), suggesting a more distributed chemical environment. Then the broadest signal was assigned to P(1) due to the first cationic shell around P being much more inhomogeneous for P(1) than P(2). In situ HT MAS NMR analyses are reported in Figure 8b. The presence of spinning sidebands (denoted with +) is explained by the high static magnetic field (14.1 T) and low spinning frequency (5 kHz) used for acquisition. From room temperature to 520 °C, no significant evolution of the two phosphorus peaks can be

dx.doi.org/10.1021/ic201572y | Inorg. Chem. 2012, 51, 4438−4447

noticed. Then, at 570 °C, the two peaks coalesce into a single broad signal centered around −4 ppm, revealing symmetry lowering from the α to the β form. Clearly, a single independent phosphorus position is expected in the β-space group. It is worthy to note the presence of a low-intensity peak at 0 ppm, coming from an impurity not detected on XRD (denoted with an asterisk). The complete reversibility of the transformation is finally highlighted on the spectrum obtained at room temperature after cooling. A preliminary model of the β phase was refined from HT-XRD data at 500 °C using the Rietveld method. The experimental resolution and maximal collected angle $2\theta_{max} = 80°$ are such that several restraints have been used for thermal parameters. Additionally, P−O distances have been restrained to 1.55(1) Å. The best agreement was obtained using the *Cm*2*a* space group (Rp = 7.70%, Rwp = 10.1%, R_{exp} = 5.32, R_{Bragg} = 10.3%, R_F = 10.4%), which corresponds to the symmetry of $Bi_2O_2(TO_3)$ (T = Te, Se) with similar arrangement between $[Bi_2O_2]^{2+}$ and O−Bi motifs. According to the NMR results, it involves only one P position in the subcell. The pertinent distances are listed in Table 4. The crystal structure of β-$Bi_4MgP_2O_{12}$ is shown in Figure 9a and 9b with the calculated/experimental XRD pattern at 500 °C. A strong rearrangement of PO_4 groups is observed between the α and β forms. In Bi_2TeO_5, the space of the tunnels is filled by the lone pairs of the TeO_3 groups, Figure 9c.

Finally, in the two novel compounds the predicted alternation of two PO_4 groups (T_d) and one excrescence (Ex) follows the (..T_d−T_d−*Ex*−...) sequence, as commonly observed for other terms of the series with the shortest ribbons ($n > 3$).[6] However, introduction of smaller Li^+ cations in the central channels can modify this sequence, e.g., in $Bi_{7.37}Li_1P_3O_{19}$ a ...−T_d−T_d−*Ex*−T_d−*Ex*−... arrangement occurs along the $[Bi_2O_2]^{2+}$ units, Figure 9d. This observation opens the door toward new arrangements within the inner space.

Electric Characterization. Even if centrosymmetric, the structural analogy between the title compounds and several ferroelectric Aurivillius compounds[10] questions the high impedance expected in this new family. Figure 10a shows the frequency dependence of the real part of the complex conductivity at different temperatures between 313 and 513 K and in the frequency range from 10^{-2} to 10^6 Hz. Measurements were performed upon heating by steps of 20 K. At high temperature two contributions of the conductivity are clearly observed, as frequency decreases, corresponding to the contribution of the bulk conductivity and the grain boundary conductivity. Thus, for T = 513 K, a first plateau observed at low frequency ($\nu \approx 10^{-2}$ Hz) in log(σ') corresponds to the dc conductivity of the grain boundary whereas a second plateau observed at higher frequency ($\nu \approx 10^2$ Hz) is attributed to the

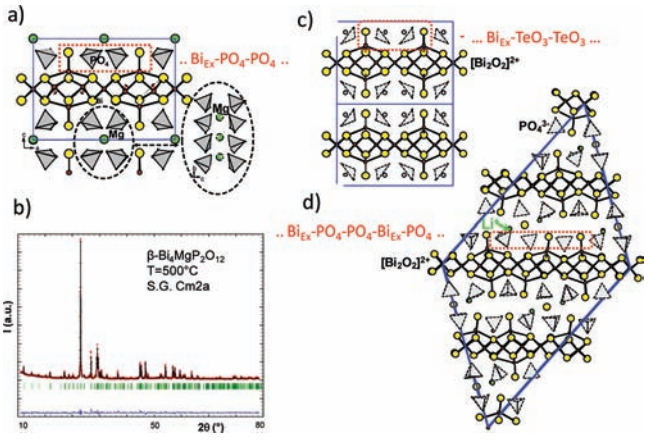

Figure 9. Crystal structure of (a) β-$Bi_4MgP_2O_{12}$ from XRD refinement at 500 °C (b), (c) $BiTe_2O_5$, and (d) $Bi_{7.37}Li_1P_3O_{19}$. Different Ex/anion sequences prove the variety of possible structural types.

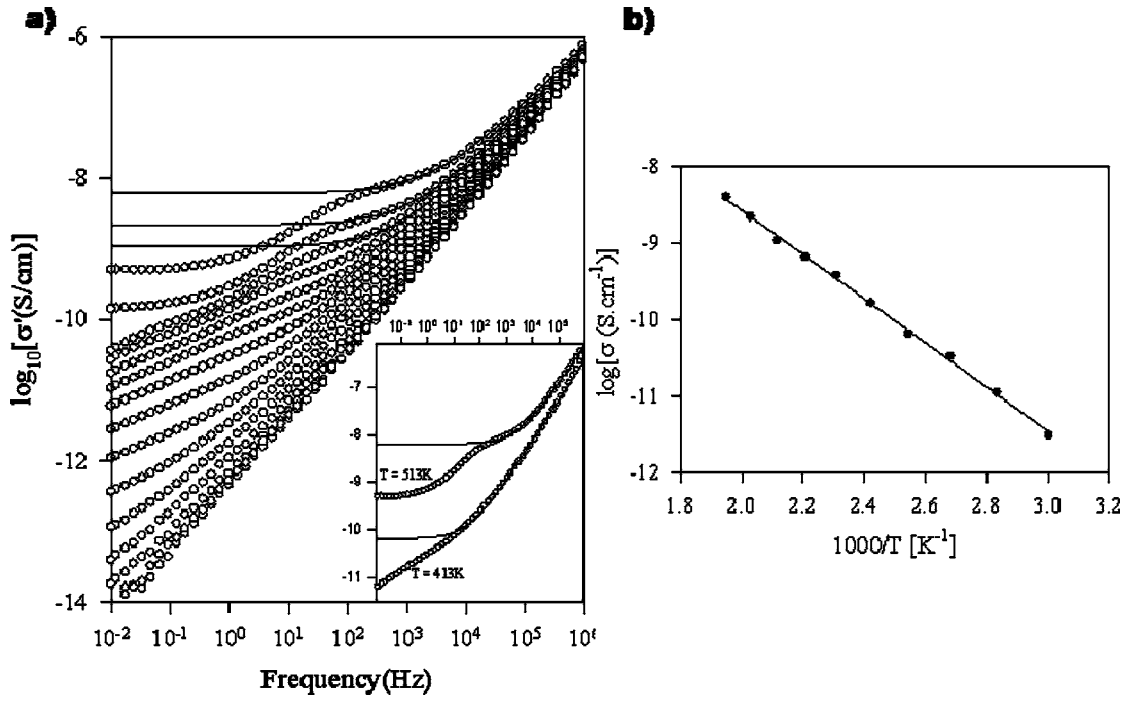

Figure 10. (a) Frequency dependence of conductivity $\sigma'(\nu)$ at different temperatures extending from 313 to 513 K by steps of 20 K. Solid lines correspond to the fit results according to eq 1. (Insert) Characteristic evolution of $\sigma'(\nu)$. (b) Temperature dependence of dc conductivity of the bulk. Solid line is the fitting according to the Arrhenius equation (eq 2).

dx.doi.org/10.1021/ic201572y | *Inorg. Chem.* 2012, 51, 4438−4447

dc conductivity of the bulk. The abrupt decrease of the conductivity between these two plateaus is related to the blocking effect of the grain boundary to the bulk charges motions. The high-frequency contribution has been fitted using the universal dielectric response expression (UDR)[33]

$$\sigma' = \sigma_{dc} + \left(\frac{\nu}{\nu^*}\right)^n \quad (1)$$

were ν^* is the cross-over frequency marking the onset of ac conduction and n $(0 < n < 1)$ a power law exponent corresponding to the high-frequency slope. ν^* and n are both temperature-dependent parameters and n increases as the temperature decreases, from the value $n = 0.8$ at 513 K to the limit value $n = 1$ at $T = 313$ K. The results of the fits are reported in Figure 10a for some characteristic temperatures, and the values of the bulk dc conductivity contribution are reported in the Arrhenius diagram of Figure 10b. The bulk dc conductivity is thermally activated and decreases as the temperature decreases by following the classical Arrhenius law

$$\sigma(T) = \sigma_o \exp\left(-\frac{E_a}{k_B T}\right) \quad (2)$$

The best fit gives for the pre-exponential factor $\sigma_o = 1.3 \times 10^{-3}$ S·cm^{-1} and for the activation energy $E_a = 0.59$ eV. The same E_a value is obtained for the low-frequency plateau, calculated from the two temperatures $T = 513$ and 493 K. These results indicate a band gap around 1.2 eV. This value is small compared to the typical values of at least 3 eV expected for insulators and suggested by the colorless feature of the crystal. Such a discrepancy can be attributed to the presence of defects which introduce deep levels in the band gap. Nevertheless, despite the existence of these defects, the conductivity remains low and suggests strongly resistant intrinsic properties and dielectric potentialities of the compound.

CONCLUSION

Starting from a series of compounds formed of 1D finite ribbons surrounded by XO_4 tetrahedral groups, we successfully predicted, formulated, and prepared the infinite homologous compound containing 2D units. They correspond to the $Bi_4MO_4(PO_4)_2$ (M = Mg, Zn) compounds. Among the two predicted hypothetical crystal structures, only one form has been obtained. It is striking that previous investigations in related chemical systems (tuning the M chemical nature) led to evidence for several discrete values for the size of the elementary ribbons (from $n = 1$ to $n = 12$ tetrahedra-wide units). Clearly, the existence of the infinite term was strongly suggested by the striking stability of so many intermediate terms. However, the stabilized crystal structure is original and complicated by important superstructure phenomena compared to the ideal models. The apparent 2D character of the prepared compounds arises from the choice of our elementary building units, namely, n-O(Bi,M)$_4$-based ribbons and PO_4 groups. In reality, strong inter-SBUs chemical bonds generate a true 3D lattices. Thus, the versatile self-assembly between the chosen units verify their pertinence in the frame of the structural prediction and could theoretically prefigure infinite megaseries. To our knowledge, the Aurivillius series displays serial arrangements between the $[Bi_2O_2]^{2+}$ entities and variably sized perovskite blocks.[34] This analogy could probably orientate the design of new compounds playing on the thickness of the sandwiched block, since the cohesion between elementary blocks is now demonstrated and fully rationalized. Also, observation of polysynthetic twinned domains by TEM outlines the flexibility of our ribbon-like units able to support local constraints, while the direction of propagation of the main structure is weakly modified. The possibility for similar but regular twin intergrowths to assemble into new polytypes also opens a broad field of new hypothetical compounds.

ASSOCIATED CONTENT

Supporting Information

Full list of atomic coordinates and distances as well as cif files. This material is available free of charge via the Internet at http://pubs.acs.org.

AUTHOR INFORMATION

Corresponding Author

*E-mail: marie.colmont@ensc-lille.fr.

Notes

The authors declare no competing financial interest.

ACKNOWLEDGMENTS

The Fonds Européeen de Développement Régional (FEDER), CNRS, Région Nord Pas-de-Calais, and Ministère de l'Education Nationale de l'Enseignement Supérieur et de la Recherche are acknowledged for funding the X-ray diffractometers. The TEM facility in Lille (France) is supported by the Conseil Regional du Nord-Pas de Calais and the European Regional Development Fund (ERDF). FEI Titan experiments were supported by the METSA program. D. Endara acknowledges the SENESCYT (Ecuadorean Government) for 3 years of Ph.D. financial support. Laurence Burylo and Nora Djellal are thanked for their precious technical help. Dr. S. Wegner and Bruker Co. are gratefully acknowledged for providing measurement time on the HT Probe.

REFERENCES

(1) Rowsell, J. L. C.; Yaghi, O. M. *Microporous Mesoporous Mater.* **2004**, *73*, 3.
(2) Ferey, G. *J. Solid State Chem.* **2000**, *152*, 37.
(3) (a) Charkin, D. O.; Kazakov, S. M.; Lebedev, D. N. *Phys. Methods Invest.* **2010**, *55*, 1323. (b) Kabbour, H.; Cario, L. *Inorg. Chem.* **2006**, *45* (6), 2713−2717.
(4) Mrotzek, A.; Kanatzidis, M. G. *Acc. Chem. Res.* **2003**, *36*,
(5) Kanatzidis, M. G. *Acc. Chem. Res.* **2005**, *38*, 359.
(6) Huvé, M.; Colmont, M.; Lejay, J.; Aschehoug, P.; Mentré, O. *Chem. Mater.* **2009**, *21*, 4019−4029.
(7) Huvé, M.; Colmont, M.; Mentré, O. *Inorg. Chem.* **2006**, *45*, 6604.
(8) O'Keeffe, M.; Eddaoudi, M.; Li, H.; Reineke, T.; Yaghi, O. M. *J. Solid State Chem.* **2000**, *152*, 3. Jansen, M. *Angew. Chem., Int. Ed.* **2002**, *41*, 3746.
(9) Siidra, O. I.; Krivovichev, S. V.; Armbruster, T; Depmeier, W. *Inorg. Chem.* **2007**, *46*, 1523−1525.
(10) (a) De Araujo, A. P.; Cuchiaro, J. D.; McMillan, L. D.; Scott, M. C.; Scott, J. F. *Nature (London)* **1995**, *374*, 627. (b) Park, H.; Kang, B. S.; Bu, S. D.; Noh, T. W.; Lee, L.; Jo, W. *Nature (London)* **1999**, *401*, 682.
(11) Damjanovic. *Curr. Opin. Solid State Mater. Sci.* **1998**, *3*, 469.
(12) (a) *SAINT+*, Version 5.00; Bruker Analytical X-ray Systems: Madison, WI, 2001. (b) *SADABS*, Version 2.03; Bruker Analytical X-ray Systems:Madison, WI, 2001 Bruker/Siemens Area detector absorption and other corrections.
(13) Petricek, V.; Dusek, M.; Palatinus, L. *JANA 2000*; Institut of Physics: Praha, Czech Republic, 2005.
(14) Huang, J.; Gu, Q.; Sleight, A. W. *J. Solid State Chem.* **1993**, *105*, 599.

(15) Abraham, F.; Ketatni, M.; Mairesse, G.; Mernari, B. *Eur. J. Solid State Chem.* **1994**, *31*, 313.
(16) Mizrahi, A.; Wignacourt, J. P.; Steinfink, H. *J. Solid State Chem.* **1997**, *133*, 516.
(17) Mizrahi, A.; Wignacourt, J. P.; Drache, M.; Conflant, P. *J. Mater.Chem.* **1995**, *5*, 901.
(18) Ketatni, M.; Mernari, B.; Abraham, F.; Mentre, O. *J. Solid State Chem.* **2000**, *153*, 48.
(19) Giraud, S.; Mizrahi, A.; Drache, M.; Conflant, P.; Wignacourt, J. P.; Steinfink, H. *Solid State Sci.* **2001**, *3*, 593.
(20) Abraham, F.; Ketatni, M.; Mernari, B. *Adv. Mater. Res.* **1994**, *1*, 223−232.
(21) Abraham, F.; Cousin, O.; Mentre, O.; Ketatni, M. *J. Solid State Chem.* **2002**, *167*, 168.
(22) Colmont, M.; Huvé, M.; Mentré, O. *Inorg. Chem.* **2006**, *45*, 6612.
(23) Steinfink, H.; Lynch, V. *J. Solid State Chem.* **2004**, *177*, 1412.
(24) Colmont, M.; Huvé, M.; Ketatni, E. M.; Mentré, O. *Solid State Sci.* **2008**, *10*, 533.
(25) Arumugam, N.; Lynch, V.; Steinfink, H. *J. Solid State Chem.* **2007**, *180*, 2690.
(26) Arumugam, N.; Lynch, V.; Steinfink, H. *J. Solid State Chem.* **2007**, *180*, 1504.
(27) Colmont, M.; Huvé, M.; Ketatni, E. M.; Abraham, F.; Mentré, O. *J. Solid State Chem.* **2003**, *176*, 221−233.
(28) Abraham, F.; Debreuille-Gresse, M. F.; Mairesse, G.; Nowogrocki, G. *Solid State Ionics.* **1988**, *529*, 28−30.
(29) Joubert, O.; Jouanneaux, A.; Ganne, M. *Nucl. Instrum. Methods Phys. Res., Sect. B* **1995**, *97*, 119.
(30) Morniroli, J. P.; Steeds, J. W. *Ultramicroscopy* **1992**, *45*, 219.
(31) Dityat'yev, O. A.; Smidt, P.; Stefanovich, S.Yu.; Lightfoot, P.; Dolgikh, V. A.; Opperman, H. *Solid State Sci.* **2004**, *6*, 915.
(32) Barsoukov, E.; Macdonald, J. R. *Impedance Spectrosc.: Theory, Exp. Appl.* **2005**.
(33) Jonscher, A. K. *Dielectric Relaxation in Solids*; Chelsea Dielectric Press, 1983.
(34) Borg, S.; Svensson, G. S.; Bovin, J. O. *J. Solid State Chem.* **2002**, *167*, 86.